ACS Photonics

Letter

pubs.acs.org/journal/apchd5

Organic Molecular Films as Light-Emitting and Light-Confining Material in Rolled-Up AlInP Semiconductor Microtube Resonators

Stefanie Kietzmann,[†] Christian Strelow,[†] Luciana Tavares,[‡] Jussi-Pekka Penttinen,[§] Teemu V. Hakkarainen,[§] Andreas Schramm,[§] Andreas Osadnik,[⊥] Arne Lützen,[⊥] Jakob Kjelstrup-Hansen,[‡] Alf Mews,[†] and Tobias Kipp*[,†]

[†]Institute of Physical Chemistry, University of Hamburg, Grindelallee 117, D-20146 Hamburg, Germany

[‡]NanoSYD, Mads Clausen Institute, University of Southern Denmark, Alsion 2, DK-6400 Sønderborg, Denmark

[§]Optoelectronics Research Centre, Tampere University of Technology, P.O. Box 692, FIN-33101 Tampere, Finland

[⊥]Kekulé-Institute of Organic Chemistry and Biochemistry, University of Bonn, Gerhard-Domagk-Straße 1, D-53121 Bonn, Germany

ABSTRACT: A hybrid inorganic/organic microcavity system is presented in which an AlInP-based rolled-up microtube resonator is combined with a thin film of naphthyl end-capped bithiophene molecules. The film is laterally structured into stripes on top of the AlInP layer system before the roll-up process. During the process, the strained bilayer together with the organic molecular stripes rolls up, and a hybrid microtube is formed. The stripes act as visible-light emitters inside the otherwise passive microtube. Furthermore, they induce a light confinement in the axial direction of the microtube, additional to the radial and azimuthal confinement that is intrinsic to a microtube. As the organic material defines the cavity and represents the emitter at the same time, an efficient light coupling into the three-dimensionally confined optical modes of the microtube resonator is ensured. The hybrid microtubes open up the opportunity for novel experiments on the light−molecule interaction as well as their application in optical components.

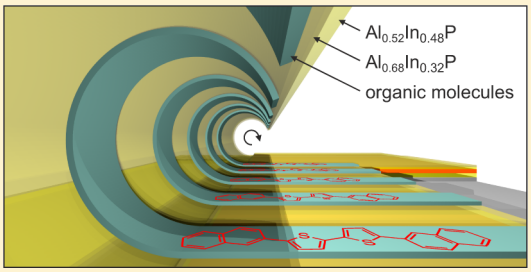

KEYWORDS: *microcavities, microtubes, AlInP, thiophenes, inorganic/organic hybrids*

Semiconductor microcavities have gained considerable interest in optical experiments due to their ability to confine light on the length scale of its wavelength. Examples of such microcavities fabricated from epitaxially grown layer systems are microdisks,[1] micropillars,[2] photonic crystals,[3] and rolled-up microtubes.[4] The latter structures are fabricated by exploiting the self-rolling mechanism of strained layer systems.[5] Microtubes can be utilized as laser cavities,[6,7] as active elements in microfluidic devices,[8] as sensors,[9] and as building blocks in lab-on-a-chip devices.[10,11]

Rolled-up microtube resonators intrinsically provide a two-dimensional confinement of light in the tube walls by waveguiding in the azimuthal direction and constructive interference. A fully tailored three-dimensional confinement can be achieved by structural variations along the tube axis, for example, of the wall thickness, the winding number, or the material composition.[7,12,13] For a coupling of light into the optical modes, emitters such as quantum dots or quantum wells can be incorporated inside the strained layer system during epitaxial growth, before the microtube is formed.[4,14,15] This approach leads to internal emitters inside the microtube; however, the epitaxial growth strongly limits the possibility to embed emitters of different material, shape, or density. On the other hand, the characteristic thin walls of optical microtube resonators also allow external emitters close to the walls to couple to the cavity modes via the modes' evanescent fields. This approach has been verified by fluid-filling of microtubes with solutions of colloidal, wet-chemically synthesized nanocrystal emitters.[16,17] Disadvantageously, here, the coupling to the optical modes is not as effective as for internal emitters; the efficiency is decreasing with increasing tube-wall thickness. A third method for coupling light emitters to the optical modes of microtube resonators is to deposit luminescent material onto the strained layer system before its lift-off from the substrate. During the lift-off process the luminescent material can be rolled into the microtube, such that for multiply rolled microtubes it is finally located inside the tube wall. Prerequisites for this method are that the luminescent material does not prevent strain relaxation during lift-off and that it withstands the sometimes rather aggressive chemistry necessary for the lift-off process. So far, this method has been successfully implemented by thermally evaporating a layer of SiO_x on top of a gradually strained epitaxial Si layer before rolling and by thermally annealing the microtubes after rolling, such that Si nanoclusters or nanocrystals are formed that give rise to luminescence in the visible spectral range.[18]

For purposes other than optical microcavity fabrication, instead of inorganic material, also organic material has been rolled up in microtubes: Self-assembled monolayers of

Received: June 25, 2015
Published: October 27, 2015

DOI: 10.1021/acsphotonics.5b00349
ACS Photonics 2015, 2, 1532−1538

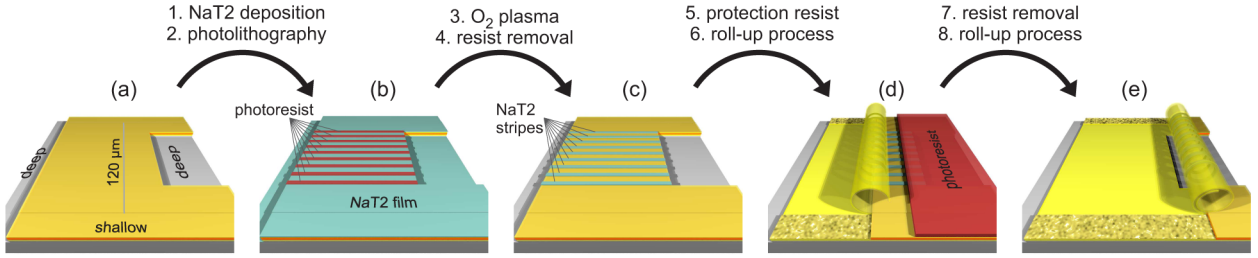

Figure 1. Sketch of the microtube sample preparation. (a) U-shaped mesa defined by deep and shallow etching. (b) NaT2 film covered by photoresist stripes. (c) NaT2 stripes. (d) Roll-up process. It temporarily stops when the microtube reaches the protection resist. (e) Final structure.

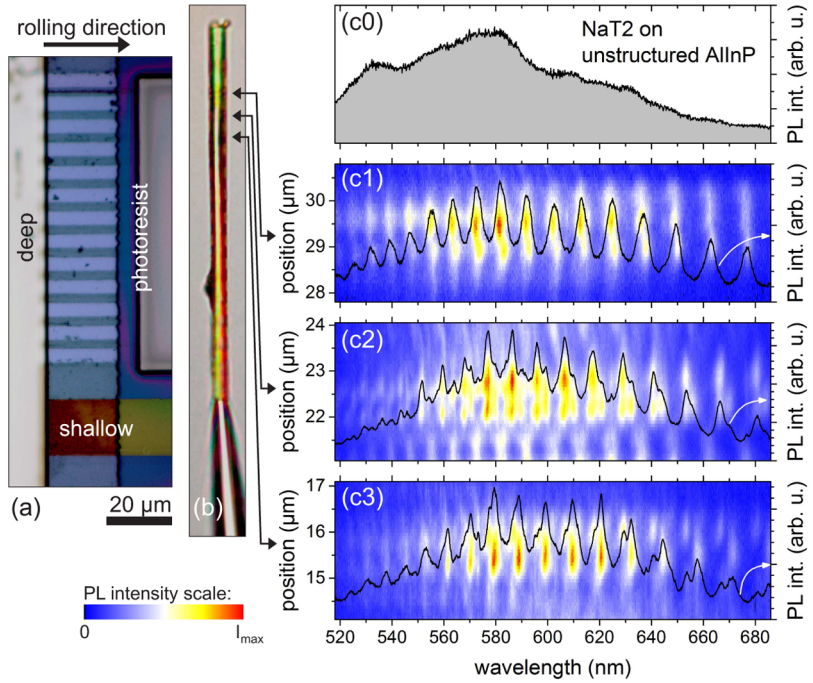

Figure 2. (a) Optical microscope image of a sample taken during the preparation process. The image corresponds to a stage between the ones sketched in Figure 1c and d, after step 5 but before step 6. (b) Microscope image of the completed microtube that is impaled on a micropipette and lifted off the substrate. (c0) PL spectrum of the NaT2 film on the planar AlInP substrate as a reference. (c1−c3) Color plots, belonging to the left vertical axes, representing spatially resolved spectra of the first three resonators of the microtube shown in (b). The black line in each of these panels represents the corresponding spatially integrated spectrum (right vertical axes).

alkenethiolate on strained layer systems have been used to fabricate radial inorganic/organic superlattices.[19,20] Alternating layers of poly(ethylenimine) and poly(acrylic acid) have been rolled up using strained semiconductor layers as templates.[21] Furthermore, polypyrrole films have been rolled up in electron-beam-evaporated strained SiO-based layer systems in order to fabricate hybrid organic/inorganic nanomembrane chemical sensors.[22]

In this work, we incorporate luminescent organic material, namely, thin films of naphthyl end-capped bithiophene molecules, into inorganic epitaxial-AlInP-based microtubes. The organic semiconductor films are laterally patterned into stripes before rolling up. Once rolled-up, these stripes act as visible-light emitting and -confining elements at the same time; thus an efficient light coupling into the microcavity is ensured. The optical modes of the hybrid inorganic/organic microtubes are probed by room-temperature photoluminescence spectroscopy and compared to results from finite-difference time-domain simulations. Our hybrid structures combine the advantages of chemically synthesized organic semiconductors and inorganic epitaxially grown materials. In organic semiconductors it is possible to tailor their electronic and optical properties just by modifying the chemical synthesis.[23] Since the performance of polymeric organic materials in general strongly depends on, for example, regioregularity and polydispersity, which makes their synthesis and purification difficult and hard to reproduce, here, we used small π-conjugated molecules that are intrinsically monodisperse and straightforward to synthesize and to purify. The vast number of structural variations around a common parent small-molecule structure enables the formation of tailored structure−properties relationships not dependent on the particular batch of the material. Furthermore, the molecules are rather easy to process, as they can be deposited on solid supports using either solution-based techniques or vapor deposition.[24,25] The advantages of the epitaxial growth are in particular the exactness and reproducibility of the emerging structures. In this work the inorganic epitaxially grown materials are used to form passive multiply rolled microtube resonators with adjustable geometries that elegantly allow the direct integration of nonepitaxially grown emitters in the mode center, a feature that is generally difficult to realize. Our work can be easily expanded by embedding, for example, quantum

DOI: 10.1021/acsphotonics.5b00349
ACS Photonics 2015, 2, 1532−1538

wells into the epitaxial layers. Together with the organic semiconductor this would lead to hybrid inorganic/organic nanostructures embedded into a (hybrid) optical microcavity. Such a system is of particular interest since in the case of resonance between the strongly localized Frenkel excitons in the organic layer, the more delocalized Wannier−Mott excitons of the quantum well, and the cavity photons, novel kinds of hybrid polaritons can emerge.[26,27]

The starting point for the preparation of the hybrid microtubes is a strained multilayer structure grown by molecular beam epitaxy, similar to those used in our previous work.[17] Grown on top of a GaAs substrate, it consists of a 200 nm GaAs buffer, 100 nm lattice-matched $Al_{0.52}In_{0.48}P$, 40 nm GaAs, 30 nm lattice-matched $Al_{0.52}In_{0.48}P$, and 20 nm tensile-strained $Al_{0.68}In_{0.32}P$. In two consecutive lithography and wet-etching processes a U-shaped mesa is defined, as is sketched in Figure 1a. First, parallel stripes in the ⟨100⟩ direction separated by 120 μm are defined by shallowly etching just through the topmost strained AlInP layer. Then, deeply etched areas are defined by etching (at least) into the 40 nm GaAs layer. The full-length deeply etched area defines the so-called starting edge, from which in the later processing the roll-up process will be initiated. The smaller area represents a depression that will be bridged by a microtube during the course of the preparation process. Until now, the preparation steps to some extent resemble our work described in ref 17; in particular, we used the same etching solutions.

After these lithographic processes, a film of 5,5′-bis(naphth-2-yl)-2,2′-bithiophene (NaT2) molecules is deposited onto the whole structured sample via sublimation of the NaT2 molecules under high-vacuum conditions ($\sim 2 \times 10^{-7}$ mbar) at an oven temperature of 583 K with a deposition rate of 0.1 Å/s and to a total thickness of 25 nm, while the substrate is kept at room temperature. NaT2 was synthesized in advance via Suzuki cross-coupling of 5,5′-dibromothiophene and 2-naphthylboronic acid as reported,[28] thereby avoiding the toxic organotin compounds used in earlier approaches.[29] In a next step, stripes of photoresist (AZ ECI 3012, MicroChemicals GmbH) perpendicular to the starting edge, with a nominal width of 2 μm and a distance of 5 μm, are defined, leading to a structure as sketched in Figure 1b. The photoresist pattern is then transferred into the NaT2 film by employing an O_2 plasma, which removes the molecule film in all uncovered areas. A conventional removal of the remaining photoresist using acetone and ultrasound is not possible without also removing the NaT2 stripes. Thus, the positive photoresist is removed by a UV exposure and subsequent development using the developer AZ 826 MIF (MicroChemicals GmbH). This developer is based on an aqueous tetramethylammonium hydroxide solution with additional surface-active agents and does not strongly affect the NaT2 stripes. The resulting structure of a strained U-shaped mesa with parallel molecular film stripes on top is sketched in Figure 1c.

In a next step, the deeply etched depression is covered by photoresist in order to protect the GaAs layer uncovered therein. An optical micrograph of a real sample in this stage of the preparation process is shown in Figure 2a. Then the sample is immersed into a solution of $NH_4OH(29.5\%)/H_2O_2(30\%)/H_2O$ (3:1:140), which selectively etches away the GaAs layer beginning from the starting edge. Consequently, the strained AlInP bilayer is lifted-off from the substrate and starts to roll up, thereby releasing parts of the tensile strain of the top AlInP layer (see Figure 1d). The rolling-up stops when the protecting photoresist is reached, while the selective undercutting of the U-shaped mesa continues as long as the sample resides in the etching solution. After the etching process the protecting photoresist is removed, again by UV exposure and subsequent development. Consequently, the roll-up process can continue as far as the bilayer is undercut, which leads to a free-standing microtube bridge across the deeply etched depression, as sketched in Figure 1e.

Free-standing microtube bridges facilitate the transfer of the tubes off the substrate. This can be accomplished by inserting a glass micropipette into the hollow core of a microtube and applying mechanical forces perpendicular to the sample surface. Figure 2b shows a micrograph of a microtube impaled on a micropipette. It is exactly the microtube that emerged upon further preparation of the sample shown in Figure 2a. The stripes of NaT2 films visible in panel (a) can, in outlines, be recognized also in panel (b) at the same vertical position. The microtube exhibits a diameter of 5.5 μm, and its wall consists of 1.85 revolutions.

The optical properties of microtubes transferred from their substrate were investigated by microphotoluminescence spectroscopy. A Ti:Sa pulsed laser, frequency-doubled to a wavelength of 445 nm, with a repetition rate of 75 MHz was focused onto NaT2-containing rings inside the microtube by a microscope objective (100×, NA = 0.8). The light emitted by the sample was collected with the same objective and imaged onto the entrance slit of a grating spectrometer. The spectrometer was equipped with a cooled charged coupled device (CCD) camera. By aligning the tube axis so that its image is parallel to the entrance slit, the two-dimensional CCD detector recorded images with spectral resolution in one direction and spatial resolution along the microtube axis in the other direction.

The false color plots in Figure 2c1−c3 represent such images obtained from three different measurements on the microtube shown in panel Figure 2b, with the excitation laser focused on the three neighboring NaT2 rings as marked in (b). Here, the laser intensity was set to 250 nW and the integration time was 30 s. Similar features are observed in all three color plots. Spatially, the emission is in each case constricted to a region smaller than 2 μm. Spectrally, a regular emission pattern occurs. Both features are typical for three-dimensionally confined modes in microtube ring or bottle resonators.[12,13] The black curve in each panel (c1)−(c3) of Figure 2 represents the spectrum that emerges by spatially integrating the color maps over the central 2 μm. Regular sequences of modes occur exhibiting some fine structure. By dividing the energy position of a peak E with its width ΔE, one obtains quality factors Q of the hybrid inorganic/organic resonators of up to 950. The envelope of all spectra resembles the emission spectrum of a NaT2 film measured on the unstructured AlInP-based layer system as depicted in Figure 2c0 for comparison. The latter in turn exhibits some rather broad spectral features that are intrinsic to the NaT2 film and that are discussed in detail in refs 28, 30, and 31.

In the following, we discuss the optical modes occurring in the hybrid microtube system in more detail. We employed three-dimensional finite-difference time-domain (FDTD) simulations using the software Lumerical FDTD. Figure 3 shows the tube geometry that was taken as the basis for the simulation. For reasons of simplicity, we simulated a tube with a length of 5 μm, centrally containing only one molecular stripe with a width of 2 μm. The diameter of the tube was set to

DOI: 10.1021/acsphotonics.5b00349
ACS Photonics 2015, 2, 1532−1538

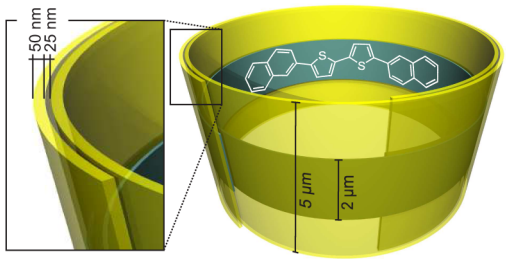

Figure 3. Sketch of the tube geometry as investigated in FDTD simulations.

5.5 μm. The inorganic part of the tube's wall consists of AlInP-based bilayers of 50 nm thickness. Their refractive index is assumed to be 3.0, following ellipsometric measurements on AlInP reported in ref 32. We note, however, that the exact value of the refractive index is not known, as it depends on the exact Al:In ratio and the remaining strain inside the wall as well as the wavelength of the propagating light wave. The molecular stripe was assumed to have a thickness of 25 nm and a refractive index of 1.7. The inorganic/organic layers were assumed to have rolled up 1.85 times; that is, the tube is 2-fold rolled over 85% of its circumference. For the FDTD simulations we placed a temporally short, thus spectrally broad, plane wave emitter pulse at a position inside the inner molecular stripe of the 2-fold rolled part. The electric field intensity is evaluated with a line monitor placed inside the 2-fold rolled part parallel to the tube axis.

Figure 4a depicts the outcome of the simulation. The electric field intensity is encoded into a color scale, while the vertical and horizontal axes give the axial position and the wavelength of light, respectively. Generally, the absolute intensities of modes calculated with the FDTD method are not directly comparable because they are dependent on the spatial overlap of both emitter and mode, as well as mode and monitor. For the depiction we, therefore, chose a simple three-color representation of the intensity as given in the color bar, which strongly emphasizes low intensities. The following observations can be made from Figure 4a: A set of spectrally sharp modes occur. These modes are axially confined roughly within the 2 μm in the middle of the simulation area that corresponds to the molecular stripe. Furthermore, they exhibit axial intensity distributions with 1 to 4 antinodes. For longer wavelengths, the spectra and the axial field distributions are quite regular and clear; here, sequences of modes with h = 1 to h = 4 antinodes can easily be distinguished, as it is seen in panel (a2), which has a magnified spectral region. For shorter wavelengths, the simulated spectrum becomes more and more chaotic.

To overcome the problem of the noncomparability of simulated mode intensities and to make the mode spectrum

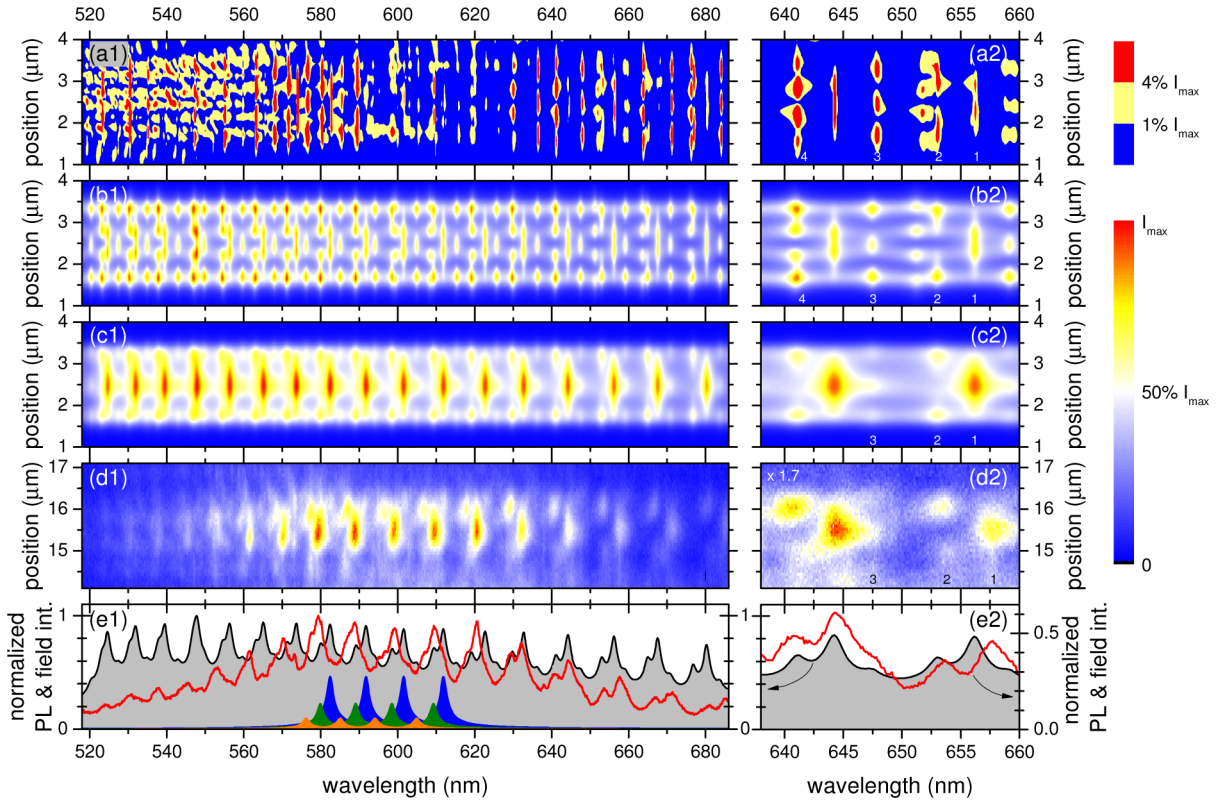

Figure 4. Results of (a–c, e) the simulations compared to the (d, e) experimental data. The panels in the left column (a1–e1) share the same extended wavelength axis. The panels in the right column (a2–e2) give a detailed view of the results in a limited wavelength region. (a) Spatially (in the axial direction) and spectrally resolved electric field intensity as calculated by FDTD simulations. The color scale is chosen to emphasize low intensities. (b) Spatially resolved mode spectrum as reconstructed from the FDTD results. (c) Further processed results of the FDTD simulations (see text). (d) Measured spatially resolved PL spectrum. The data are the same as depicted in Figure 2c3. The color scales in (d1) and (d2) are the same, but the measured intensity in (d2) is multiplied by 1.7 to account for the lower signal in the depicted wavelength region. (e) Comparison between simulated (black curve) and measured (red curve) spectrum obtained by spatially integrating the color plots in (c) and (d), respectively. The colored and filled Lorentzian curves in (e1) represent some of the individual modes that, when all summed up, result in the black curve.

DOI: 10.1021/acsphotonics.5b00349
ACS Photonics 2015, 2, 1532–1538

clearer, we further evaluated the simulated results. All visible modes were categorized by their axial mode number h = 1, 2, 3, 4, and their energy positions were read out. Furthermore, for exemplary modes of each h, the axial field distributions, i.e., vertical cross sections in Figure 4a, have been derived. Finally, the Q factors of several of the simulated modes have been determined. For the modes in the longer wavelength region between 676 and 685 nm, Q factors of about 4250, 3850, 3550, and 2550 for h = 1, 2, 3, and 4 occur, respectively. The decrease of the Q factor for increasing mode numbers is a general feature and can be explained by stronger losses for those modes that are located closer to the edges of the molecular film stripe. By assuming a Lorentzian spectral distribution of each mode and by using the list of mode positions and widths together with the corresponding normalized spatial mode distributions as read out from Figure 4a, a new color plot of the spatial and spectral mode distribution can be compiled. Such a plot is shown in Figure 4b, where we assumed Q = 4000 for all modes for the sake of simplicity. Of course, general features of the direct depiction of the FDTD simulations in panel (a) reoccur; however the representation of the modes is more tidy.

For comparison, Figure 4d shows the experimentally obtained spatially resolved spectra already depicted in Figure 2c3. It becomes obvious that the simulated data exhibit more and sharper modes with a larger axial extension. The measurement reveals a dominant sequence of modes with a single antinode in the axial direction. The corresponding sequence in the simulation has approximately the same mode spacing. A further sequence of modes with two antinodes is also clearly visible in the measurements. Unlike the simulation, these modes exhibit a slightly asymmetric axial field distribution. The mode spacing between neighboring modes with h = 1 and h = 2 is slightly larger in the measurement than in the simulation. Modes with h = 3 are only allusively recognizable (cf. Figure 4d2), while modes with h = 4 are not resolvable at all, in contrast to the simulations, where both sequences are prominent.

Differences between simulation and measurement occur most likely because of deviations and imperfections of the real hybrid microtube structure compared to the model structure. The generally broader modes of the measurements can, for example, be caused by additional losses induced by scattering on surface roughness of the NaT2 stripes or by reabsorption of light. The slightly larger mode spacing between h = 1 and h = 2 modes hint at a smaller NaT2-stripe width than assumed during the simulation. The only faint appearance of h = 3 modes can be explained by the fact that higher axial modes are more prone to structural imperfections at the NaT2-stripe edges, which in turn might significantly dampen those modes. The absence of modes with h = 4 in the measurements, which still occur in the simulations, also rationalizes a smaller resonator width or very strong damping of those modes.

We further processed the results of the FDTD simulations to better reproduce the measurement. First an upper limit of the Q factor for all modes of 1800 was assumed. To account for the different coupling efficiencies of the excited emitters to the different axial modes as observed experimentally, we weighted the sequences with h = 1, 2, and 3 before superimposing them. We assumed the h = 2 and h = 3 modes contribute 50% and 20% of the h = 1 sequence, respectively. We neglected the h = 4 sequence. The resulting spatially resolved spectrum of the simulation depicted in Figure 4c reveals strong similarities to the measured spectrum shown in panel (d). Note that the general decrease of the measured intensity to smaller and higher wavelengths, which is an intrinsic and characteristic feature of the NaT2 emitters (see Figure 2c0), is not visible in the simulations since a spectrally constant emitter has been assumed.

The choice of the limiting Q factor and the weighting factors for the different axial modes seems to be fairly arbitrary. However, one interesting feature is hidden behind the choice of parameters. If one spatially integrates the simulated data in Figure 4c, the gray-filled spectrum shown in Figure 4e is obtained. The red curve corresponds to the measured spatially integrated spectrum. Both spectra are normalized to their maxima. In particular in the center spectral region not only the shape of the spectra but also the relative intensities are fairly similar. For a better insight, in panel (e1) also the intensities of the individual modes with different h and weighting, which sum up to the gray-filled spectrum, are shown in the central wavelength region. If one assumes lower Q factors for these simulated modes, they would broaden and merge into a total spectrum with a considerably lower modulation of the intensity, which is in contrast to the measurement. Increasing the weight of the h = 2 and h = 3 modes would also result in a lower modulation of the intensity. A compensation of this by assuming higher Q factors, on the other hand, is not reasonable regarding the measured mode widths. This shows that the possible choice of Q and weighting factors is acceptable only within narrow limits. A further implication of the preceding analysis concerns the background of the measured spectra. From the measurement alone, one might think that the modes are superimposed on a considerable strong background emission, i.e., emission from so-called leaky modes that are not waveguided by the microtube. However, in contrast, the simulations prove that such a background emission is negligibly small. The alleged background is just a result of the merging of different neighboring modes.

In summary, we have fabricated hybrid inorganic/organic microtube resonatores by rolling up stripes of NaT2 films in an AlInP-based microtube. The inorganic semiconductor part alone is optically passive in the visible wavelength regime. The organic molecular stripes are acting as visible-light emitters. Furthermore, they induce a structural variation of the material in the axial direction of the microtube system that leads to a three-dimensional confinement of light. Since the molecules represent light-emitting and light-confining material at the same time, an efficient coupling into the resonant cavity modes occurs. The direct integration of molecular emitters in the mode center of microtube resonators, which is rendered possible by the peculiar fabrication process, opens up new perspectives for future experiments on light−molecule interactions and for possible applications of these hybrid structures as active, wavelength-selective components. The combination of epitaxially grown inorganic and chemically synthesized organic semiconductors also directly allows for the fabrication of hybrid inorganic/organic excitonic nanostructures with interesting properties for basic science as well as for applications. In our approach, one can, for example, easily integrate quantum wells inside the strained AlInP-based layer system. Resonant coupling of loosely bound and extended Wannier−Mott excitons in quantum wells to tightly bound and localized Frenkel excitons in the organic layer can lead to hybrid quantum systems exhibiting, for example, high oscillator strengths and strong optical nonlinearities.[26] The inorganic material can also be exploited for an efficient injection of charge

DOI: 10.1021/acsphotonics.5b00349
ACS Photonics 2015, 2, 1532−1538

carriers into the structure, while the organic semiconductor part exhibits strong light−matter coupling and possibly a high fluorescence yield.[33,34] Placing such hybrid excitonic systems into an optical microcavity just by rolling it up into a microtube might lead to an interesting platform for the investigation of new polaritonic effects[27] and the development of novel light-emitting or nonlinear-optical devices.

AUTHOR INFORMATION

Corresponding Author

*E-mail: kipp@chemie.uni-hamburg.de.

Notes

The authors declare no competing financial interest.

ACKNOWLEDGMENTS

This work is funded by the Deutsche Forschungsgemeinschaft via Grant No. KI 1257/1. We furthermore acknowledge support by the Landesforschungsförderung of the Freie und Hansestadt Hamburg. L.T. thanks the Danish Council for Independent Research | Technology and Production Sciences for financial support (FTP Contract No. 12-132326).

REFERENCES

(1) McCall, S. L.; Levi, A. F. J.; Slusher, R. E.; Pearton, S. J.; Logan, R. A. Whispering-gallery mode microdisk lasers. *Appl. Phys. Lett.* **1992**, *60*, 289−291.

(2) Gérard, J. M.; Barrier, D.; Marzin, J. Y.; Kuszelewicz, R.; Manin, L.; Costard, E.; Thierry-Mieg, V.; Rivera, T. Quantum boxes as active probes for photonic microstructures: The pillar microcavity case. *Appl. Phys. Lett.* **1996**, *69*, 449−451.

(3) Painter, O.; Lee, R. K.; Scherer, A.; Yariv, A.; O'Brien, J. D.; Dapkus, P. D.; Kim, I. Two-Dimensional Photonic Band-Gap Defect Mode Laser. *Science* **1999**, *284*, 1819−1821.

(4) Kipp, T.; Welsch, H.; Strelow, C.; Heyn, C.; Heitmann, D. Optical Modes in Semiconductor Microtube Ring Resonators. *Phys. Rev. Lett.* **2006**, *96*, 077403.

(5) Prinz, V. Y.; Seleznev, V. A.; Gutakovsky, A. K.; Chehovskiy, A. V.; Preobrazhenskii, V. V.; Putyato, M. A.; Gavrilova, T. A. Free-standing and overgrown InGaAs/GaAs nanotubes, nanohelices and their arrays. *Phys. E (Amsterdam, Neth.)* **2000**, *6*, 828−831.

(6) Li, F.; Mi, Z. Optically pumped rolled-up InGaAs/GaAs quantum dot microtube lasers. *Opt. Express* **2009**, *17*, 19933.

(7) Strelow, C.; Sauer, M.; Fehringer, S.; Korn, T.; Schüller, C.; Stemmann, A.; Heyn, C.; Heitmann, D.; Kipp, T. Time-resolved studies of a rolled-up semiconductor microtube laser. *Appl. Phys. Lett.* **2009**, *95*, 221115.

(8) Thurmer, D. J.; Deneke, C.; Mei, Y.; Schmidt, O. G. Process integration of microtubes for fluidic applications. *Appl. Phys. Lett.* **2006**, *89*, 223507.

(9) Bolaños Quiñones, V. A.; Ma, L.; Li, S.; Jorgensen, M.; Kiravittaya, S.; Schmidt, O. G. Localized optical resonances in low refractive index rolled-up microtube cavity for liquid-core optofluidic detection. *Appl. Phys. Lett.* **2012**, *101*, 151107.

(10) Harazim, S. M.; Bolaños Quiñones, V. A.; Kiravittaya, S.; Sanchez, S.; Schmidt, O. G. Lab-in-a-tube: on-chip integration of glass optofluidic ring resonators for label-free sensing applications. *Lab Chip* **2012**, *12*, 2649−2655.

(11) Smith, E. J.; Xi, W.; Makarov, D.; Mönch, I.; Harazim, S.; Bolaños Quiñones, V. A.; Schmidt, C. K.; Mei, Y.; Sanchez, S.; Schmidt, O. G. Lab-in-a-tube: ultracompact components for on-chip capture and detection of individual micro-/nanoorganisms. *Lab Chip* **2012**, *12*, 1917−1931.

(12) Strelow, C.; Rehberg, H.; Schultz, C. M.; Welsch, H.; Heyn, C.; Heitmann, D.; Kipp, T. Optical Microcavities Formed by Semiconductor Microtubes Using a Bottlelike Geometry. *Phys. Rev. Lett.* **2008**, *101*, 127403.

(13) Strelow, C.; Schultz, C. M.; Rehberg, H.; Sauer, M.; Welsch, H.; Stemmann, A.; Heyn, C.; Heitmann, D.; Kipp, T. Light confinement and mode splitting in rolled-up semiconductor microtube bottle resonators. *Phys. Rev. B: Condens. Matter Mater. Phys.* **2012**, *85*, 155329.

(14) Strelow, C.; Schultz, C. M.; Rehberg, H.; Welsch, H.; Heyn, C.; Heitmann, D.; Kipp, T. Three dimensionally confined optical modes in quantum-well microtube ring resonators. *Phys. Rev. B: Condens. Matter Mater. Phys.* **2007**, *76*, 045303.

(15) Li, F.; Vicknesh, S.; Mi, Z. Optical modes in InGaAs/GaAs quantum dot microtube ring resonators at room temperature. *Electron. Lett.* **2009**, *45*, 645−646.

(16) Dietrich, K.; Strelow, C.; Schliehe, C.; Heyn, C.; Stemmann, A.; Schwaiger, S.; Mendach, S.; Mews, A.; Weller, H.; Heitmann, D.; Kipp, T. Optical Modes Excited by Evanescent-Wave-Coupled PbS Nanocrystals in Semiconductor Microtube Bottle Resonators. *Nano Lett.* **2010**, *10*, 627−631.

(17) Strelow, C.; Kietzmann, S.; Schramm, A.; Seher, R.; Penttinen, J.-P.; Hakkarainen, T. V.; Mews, A.; Kipp, T. AlInP-based rolled-up microtube resonators with colloidal nanocrystals operating in the visible spectral range. *Appl. Phys. Lett.* **2012**, *101*, 113114.

(18) Songmuang, R.; Rastelli, A.; Mendach, S.; Schmidt, O. G. SiOx/Si radial superlattices and microtube optical ring resonators. *Appl. Phys. Lett.* **2007**, *90*, 091905.

(19) Deneke, C.; Zschieschang, U.; Klauk, H.; Schmidt, O. G. InGaAs/GaAs/alkanethiolate radial superlattices. *Appl. Phys. Lett.* **2006**, *89*, 263110.

(20) Bof Bufon, C. C.; Arias Espinoza, J. D.; Thurmer, D. J.; Bauer, M.; Deneke, C.; Zschieschang, U.; Klauk, H.; Schmidt, O. G. Hybrid Organic/Inorganic Molecular Heterojunctions Based on Strained Nanomembranes. *Nano Lett.* **2011**, *11*, 3727−3733.

(21) Todaro, M. T.; Blasi, L.; Giordano, C.; Rizzo, A.; Cingolani, R.; Gigli, G.; Passaseo, A.; De Vittorio, M. Nanowalled polymer microtubes fabricated by using strained semiconductor templates. *Nanotechnology* **2010**, *21*, 245305.

(22) Vervacke, C.; Bufon, C. C. B.; Thurmer, D. J.; Schmidt, O. G. Three-dimensional chemical sensors based on rolled-up hybrid nanomembranes. *RSC Adv.* **2014**, *4*, 9723−9729.

(23) Köhler, A.; Bässler, H. *Electronic Processes in Organic Semiconductors: An Introduction*; Wiley-VCH: Weinheim, 2015.

(24) Müllen, K.; Wegner, G., Eds. *Electronic Materials: The Oligomer Approach*; Wiley-VCH Verlag GmbH, 1998.

(25) Mishra, A.; Bäuerle, P. Small Molecule Organic Semiconductors on the Move: Promises for Future Solar Energy Technology. *Angew. Chem., Int. Ed.* **2012**, *51*, 2020−2067.

(26) Agranovich, V. M.; Gartstein, Y. N.; Litinskaya, M. Hybrid Resonant Organic−Inorganic Nanostructures for Optoelectronic Applications. *Chem. Rev.* **2011**, *111*, 5179−5214.

(27) Slootsky, M.; Liu, X.; Menon, V. M.; Forrest, S. R. Room Temperature Frenkel-Wannier-Mott Hybridization of Degenerate Excitons in a Strongly Coupled Microcavity. *Phys. Rev. Lett.* **2014**, *112*, 076401.

(28) Liu, X.; Wallmann, I.; Boudinov, H.; Kjelstrup-Hansen, J.; Schiek, M.; Lützen, A.; Rubahn, H.-G. AC-biased organic light-emitting field-effect transistors from naphthyl end-capped oligothiophenes. *Org. Electron.* **2010**, *11*, 1096−1102.

(29) Tian, H. K.; Shi, J. W.; He, B.; Hu, N. H.; Dong, S. Q.; Yan, D. H.; Zhang, J. P.; Geng, Y. H.; Wang, F. S. Naphthyl and Thionaphthyl End-Capped Oligothiophenes as Organic Semiconductors: Effect of Chain Length and End-Capping Groups. *Adv. Funct. Mater.* **2007**, *17*, 1940−1951.

(30) Liu, X.; Tavares, L.; Osadnik, A.; Lausen, J. L.; Kongsted, J.; Lützen, A.; Rubahn, H.-G.; Kjelstrup-Hansen, J. Low-voltage organic phototransistors based on naphthyl end-capped oligothiophene nanofibers. *Org. Electron.* **2014**, *15*, 1273−1281.

(31) Balzer, F.; Schiek, M.; Osadnik, A.; Wallmann, I.; Parisi, J.; Rubahn, H.-G.; Lützen, A. Substrate steered crystallization of naphthyl end-capped oligothiophenes into nanofibers: the influence of methoxy-functionalization. *Phys. Chem. Chem. Phys.* **2014**, *16*, 5747−5754.

DOI: 10.1021/acsphotonics.5b00349
ACS Photonics 2015, 2, 1532−1538

(32) Diedenhofen, S. L.; Grzela, G.; Haverkamp, E.; Bauhuis, G.; Schermer, J.; Rivas, J. G. Broadband and omnidirectional anti-reflection layer for III/V multi-junction solar cells. *Sol. Energy Mater. Sol. Cells* **2012**, *101*, 308−314.
(33) Chanyawadee, S.; Lagoudakis, P. G.; Harley, R. T.; Lidzey, D. G.; Henini, M. Nonradiative exciton energy transfer in hybrid organic-inorganic heterostructures. *Phys. Rev. B: Condens. Matter Mater. Phys.* **2008**, *77*, 193402.
(34) Schlesinger, R.; Bianchi, F.; Blumstengel, S.; Christodoulou, C.; Ovsyannikov, R.; Kobin, B.; Moudgil, K.; Barlow, S.; Hecht, S.; Marder, S. R.; Henneberger, F.; Koch, N. Efficient light emission from inorganic and organic semiconductor hybrid structures by energy-level tuning. *Nat. Commun.* **2015**, *6*, 675410.1038/ncomms7754.

DOI: 10.1021/acsphotonics.5b00349
ACS Photonics 2015, 2, 1532−1538